Valence fluctuation in Ce$_2$Re$_3$Si$_5$ and Ising-type magnetic ordering in Pr$_2$Re$_3$Si$_5$ single crystals

Suman Sanki [ORCID],[1] Vikash Sharma,[1] Souvik Sasmal [ORCID],[1] Vikas Saini [ORCID],[1] Gourav Dwari [ORCID],[1] Bishal Baran Maity,[1] Ruta Kulkarni,[1] Ram Prakash Pandeya,[1] Rajib Mondal [ORCID],[2] Achintya Lakshan,[3] Sitaram Ramakrishnan [ORCID],[4] Partha Pratim Jana,[3] Kalobaran Maiti,[1] and A. Thamizhavel [ORCID][1,*]

[1]*Department of Condensed Matter Physics and Materials Science, Tata Institute of Fundamental Research, Homi Bhabha Road, Colaba, Mumbai 400 005, India*

[2]*UGC-DAE Consortium for Scientific Research, Kolkata Centre, Bidhannagar, Kolkata 700 106, India*

[3]*Department of Chemistry, IIT Kharagpur, Kharagpur 721302, India*

[4]*Department of Quantum Matter, Hiroshima University, 739-8530 Higashi-Hiroshima, Japan*

Single crystals of Ce$_2$Re$_3$Si$_5$ and Pr$_2$Re$_3$Si$_5$ have been grown by the Czochralski method in a tetra-arc furnace. Powder x-ray diffraction confirmed that these compounds crystallize in the U$_2$Mn$_3$Si$_5$-type tetragonal crystal structure with space group $P4/mnc$ (no. 128). The anisotropic physical properties have been studied comprehensively by measuring the magnetic susceptibility, isothermal magnetization, electrical transport, and specific heat. The low value of magnetic susceptibility together with no magnetic transition down to 2 K and the observation of the signature of the Kondo feature in the photoemission spectra provide evidence that the Ce ions are in the intermediate valence state in Ce$_2$Re$_3$Si$_5$. On the other hand, Pr$_2$Re$_3$Si$_5$ revealed a magnetic ordering at 9 K. The sharp drop in the magnetic susceptibility and a spin-flip-like metamagnetic transition for $H \parallel [001]$ in the magnetization plot of Pr$_2$Re$_3$Si$_5$ suggest an Ising-type antiferromagnetic ordering. Based on magnetic susceptibility and isothermal magnetization data, a detailed crystal electric field (CEF) analysis shows that the degenerate $\boldsymbol{J} = 4$ Hund's rule derived ground state of a Pr^{3+} ion splits into nine singlets with an overall splitting of 1179 K. The magnetic ordering in Pr$_2$Re$_3$Si$_5$ is due to the exchange-generated admixture of the lowest-lying CEF energy levels. Heat capacity data reveal a sharp peak at 9 K, which confirms the bulk nature of the magnetic ordering in Pr$_2$Re$_3$Si$_5$.

I. INTRODUCTION

The physical properties of rare-earth-based intermetallic compounds are fascinating due to their localized nature of 4f electrons, where the Ruderman, Kittel, Kasuya, and Yosida (RKKY) interaction leads to magnetic ordering [1,2]. Of all the rare-earth intermetallic compounds, the Ce-based intermetallic compounds show the most interesting properties, such as magnetic ordering, valence fluctuation, the Kondo effect, quantum criticality, heavy fermionic behavior, unconventional superconductivity, etc. [3–8]. It is well documented in the literature that the reason for those anomalous physical properties in Ce compounds is due to the close proximity of the 4f level to the Fermi energy E_F, which results in the hybridization of conduction electrons with the localized 4f electrons. When there is a strong hybridization of the conduction electrons with 4f electrons, it results in a weaker localization of the 4f electrons, and the system becomes nonmagnetic or a mixed valent state. Pr-based compounds also exhibit interesting physical properties, such as spin-glass behavior, heavy-fermion superconductivity, antiferroquadrupolar ordering, etc. [9–12]. In this manuscript,

we present the anisotropic physical properties of R_2Re$_3$Si$_5$ ($R =$ Ce and Pr) single crystals.

The rare-earth intermetallic compounds having the general formula $R_2T_3X_5$, where R denotes rare earth, T denotes transition metal, and $X =$ Si or Ge, are often referred to as 2-3-5 compounds, and they adopt either a tetragonal or orthorhombic crystal structure [13,14]. In this series of 2-3-5 compounds, both Ce and Pr compounds show interesting physical properties. For example, Ce$_2$Ni$_3$Ge$_5$, which crystallizes in the orthorhombic crystal structure, is an antiferromagnet with two magnetic transitions at $T_{N1} = 5$ K and $T_{N2} = 4.3$ K as inferred from a single crystalline study [15], and it becomes a pressure-induced superconductor in the critical pressure range 3.4–3.9 GPa [16]. The other germanides, such as Ce$_2$Pd$_3$Ge$_5$, Ce$_2$Rh$_3$Ge$_5$, and Ce$_2$Ir$_3$Ge$_5$, are antiferromagnets [17,18], while their Si counterparts are either intermediate valent or nonmagnets [17,19]. Similarly, Pr-based 2-3-5 compounds show magnetic ordering and superconductivity at low temperature, and they have been studied in polycrystalline form [20,21]. Due to the interesting physical properties in these 2-3-5 compound series, we have made an attempt to grow the single crystal of R_2Re$_3$Si$_5$ ($R =$ Ce and Pr). Except for the crystal structure information, the magnetic properties of these systems have not been studied so far. These compounds crystallize in U$_2$Mn$_3$Si$_5$-type tetragonal crystal structure with space group $P4/mnc$ (no. 128) [22].

*Corresponding author: thamizh@tifr.res.in

From the magnetic susceptibility and transport measurements, we find that $Ce_2Re_3Si_5$ does not show any magnetic ordering down to 2 K, and from the analysis of magnetic susceptibility we conclude that the Ce atom is in its intermediate valent state. On the other hand, $Pr_2Re_3Si_5$ shows a clear magnetic ordering at 9 K, which is confirmed from the magnetic susceptibility, electrical resistivity and heat capacity studies.

II. EXPERIMENT

Single crystals of $R_2Re_3Si_5$ (R = Ce and Pr) have been grown directly from its melt by the Czochralski method in a tetra-arc furnace (Technosearch Corp., Japan) under an argon atmosphere. At first, a polycrystalline ingot of about 10 g was prepared from the high-purity starting elements of Ce, Re, and Si in the molar ratio 2:3:5. A polycrystalline seed was cut from the ingot for the growth of a single crystal. The ingot was melted completely and the polycrystalline seed was carefully inserted into the melt and pulled at a speed of 50 mm/h. Once a steady-state condition was achieved, the pulling speed was reduced to 10 mm/h for the entire growth of the single crystal. About 70-mm-long crystal was pulled with a typical diameter of 3–4 mm. From the Laue diffraction pattern, we confirmed that the crystal was growing along the [001] direction. The stoichiometry of the grown crystal was confirmed from the energy-dispersive analysis by x-ray (EDAX). Powder x-ray diffraction (PXRD) studies were performed in a PANalytical x-ray diffractometer that is equipped with a Cu $K\alpha$ monochromatic source. Single-crystal x-ray diffraction (SXRD) for $Ce_2Re_3Si_5$ was measured on a four-circle Bruker diffractometer employing Mo $K\alpha$ radiation. Refer to the supplemental material [23] for details. X-ray photoelectron spectroscopy (XPS) measurement was performed on an *in situ* cleaved single-crystalline sample of $Ce_2Re_3Si_5$ using a Gammadata Scienta R4000 WAL electron analyzer attached with a monochromatic Al $K\alpha$–photon source. The single crystalline nature of the crystal was confirmed from the Laue diffraction and aligned along the principal crystallographic directions. The oriented crystals were cut along the two principal crystallographic directions by a wire electric discharge machine. Magnetic susceptibility and magnetization measurements were performed in a magnetic property measurement system (MPMS), Quantum Design, USA, and the electrical resistivity and heat capacity measurements were performed in a physical property measurement system (PPMS), Quantum Design, USA.

III. RESULTS AND DISCUSSION

A. X-ray diffraction studies of $Ce_2Re_3Si_5$ and $Pr_2Re_3Si_5$

The crystal structure of $Ce_2Re_3Si_5$ is shown Fig. 1(a). The Ce atoms in the unit cell are arranged in a rectangular network with a nearest-neighboring distance of 3.867 Å. The rare-earth atom occupies the 8*h* Wyckoff's position; there are two different sites for the Re atom, namely 8*h* and 4*d*, while Si atoms occupy 8*h*, 8*g*, and 4*e*. The unit cell contains 4 formula units with 40 atoms. To check the phase purity of the grown crystal and to estimate the lattice constants, a small portion of the crystal was ground to a fine powder and subjected to room-temperature PXRD. The Rietveld analysis performed on
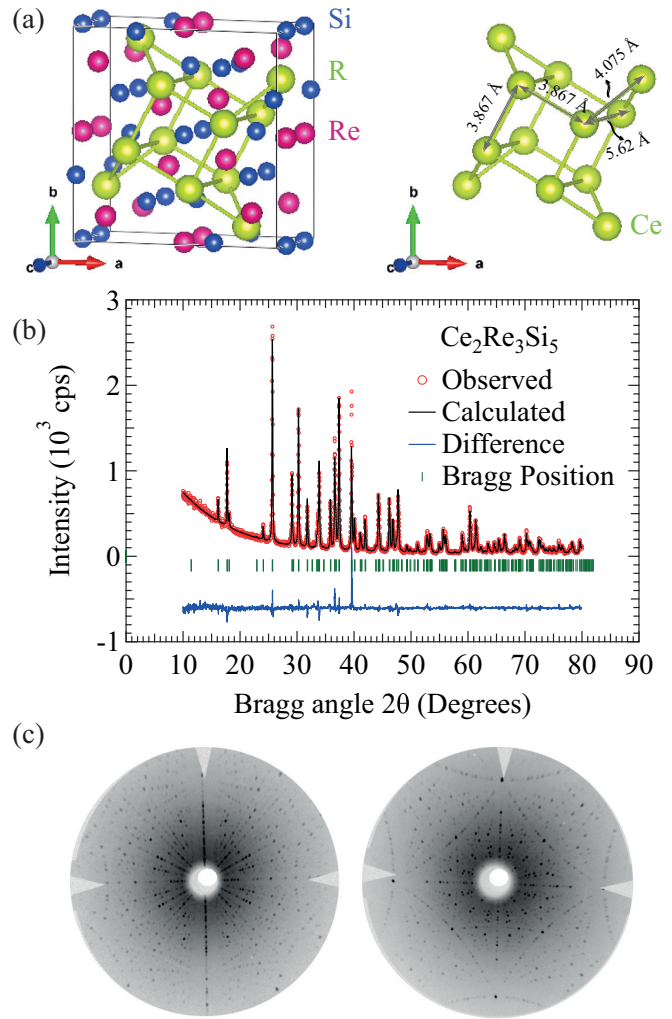

FIG. 1. (a) Crystal structure of $R_2Re_3Si_5$ (R = Ce and Pr) depicting the unit cell and arrangement of the rare-earth atom in the unit cell. (b) Powder x-ray diffraction pattern along with the Rietveld refinement of $Ce_2Re_3Si_5$. (c) Laue diffraction pattern corresponding to the (100) and (001) plane.

the PXRD pattern using the FULLPROF software package [24] is shown in Fig. 1(b). We have estimated the lattice parameters of $Ce_2Re_3Si_5$ as a = 10.975(2) Å and c = 5.627(1) Å, which are in good agreement with the reported values [25]. The unit-cell volume of $Ce_2Re_3Si_5$ is estimated as 677.78 Å^3. Similarly, we have estimated the lattice constants of $Pr_2Re_3Si_5$ from the PXRD data. The obtained lattice parameters for $Pr_2Re_3Si_5$ are a = 10.994(3) Å and c = 5.687(6) Å, and the volume of the unit cell amounts to 687.37 Å^3. Typically, in rare-earth compounds one would expect a reduction in the unit-cell volume as we move down in the rare-earth element. Here the unit-cell volume of $Pr_2Re_3Si_5$ is larger than that of $Ce_2Re_3Si_5$. This suggests that $Ce_2Re_3Si_5$ may exist in a tetravalent or valence fluctuating state. Next, we performed Laue diffraction, in backreflection geometry, on a cut piece of the single crystal, and the obtained Laue diffraction pattern corresponding to the principal planes, viz., (100) and (001), are shown in Fig. 1(c). The well-defined Laue diffraction pattern together with the fourfold symmetry indicate a good

TABLE I. Atomic coordinates x, y, z and atomic displacement parameters (ADPs) of $Ce_2Re_3Si_5$ at room temperature in $Å^2$. Unique reflections (obs/all) = 837/855, criterion of observability: $I > 3\sigma(I)$, R_F(obs/all) = 0.0219/0.0225, no. of parameters is 31. Refinement method used: least-squares on F. Space group: $P4/mnc$.

Atom	Wyck	Occ.	x	y	z	U_{11}	U_{22}	U_{33}	U_{12}	U_{13}	U_{23}	U_{iso}^{eq}
Ce	8h	1	0.2623(1)	0.4250(1)	0	0.0043(2)	0.0069(2)	0.0022(2)	−0.0003(1)	0	0	0.0045(1)
Re1	8h	1	0.1445(1)	0.1234(1)	0	0.0035(1)	0.0040(1)	0.0026(1)	−0.0001(1)	0	0	0.0034(1)
Re2	4d	1	0	0.5	0.25	0.0041(1)	0.0041	0.0024(2)	0.0006(1)	0	0	0.0035(1)
Si1	8h	1	0.0242(2)	0.3161(2)	0	0.0034(7)	0.0048(7)	0.0035(7)	−0.0011(6)	0	0	0.0039(4)
Si2	8g	1	0.1732(1)	0.6732	0.25	0.0040(4)	0.0040	0.0063(8)	−0.0013(6)	−0.0036(4)	0.0036	0.0047(3)
Si3	4e	1	0	0	0.2522(5)	0.0056(7)	0.0056	0.0032(10)	0	0	0	0.0048(4)

quality of the single crystal. From the SXRD analysis we find $Ce_2Re_3Si_5$ to be perfectly ordered, unlike in the case of the isostructural compound $Ce_2Ru_3Ga_5$, where there is a site exchange between Ru and Ga at the 4d site [26]. SXRD data were processed with APEX-III software [27]. The structure refinement was done using JANA 2006 [28]. Table I shows the atomic coordinates at room temperature for the ordered structure. For additional details, see Ref. [23].

B. Physical properties of $Ce_2Re_3Si_5$

In this section, we discuss the physical properties of $Ce_2Re_3Si_5$. The temperature dependence of the dc magnetic susceptibility of $Ce_2Re_3Si_5$ measured along the two principal crystallographic directions, in a field of 5 kOe, in the temperature range from 1.8 to 300 K is shown in the main panel of Fig. 2. The susceptibility depicts a weak temperature dependence down to 50 K followed by an increase at low temperature. The nearly temperature-independent susceptibility, with a relatively small value in the temperature range 100–300 K together with a nonmagnetic ground state, suggest that the $4f$ electrons of the Ce atom are in the valence fluctuating state. An estimate of the effective magnetic moment was done from the modified Curie-Weiss law

FIG. 2. Temperature dependence of magnetic susceptibility of $Ce_2Re_3Si_5$ along the two principal crystallographic directions. The inset shows the inverse susceptibility, and the solid lines correspond to the fit to the ICF model (see the text for details).

$\chi^{-1} = [\chi_0 + \mu_{eff}^2/8(T - \theta_p)]^{-1}$ in the temperature range 200–300 K. The effective magnetic moments thus obtained are 0.25 and 0.20 μ_B/Ce, respectively, for the [100] and [001] directions. Ideally, for a cerium atom in its trivalent state one would expect the effective magnetic moment to be 2.54 μ_B/Ce, and for a tetravalent state 0 μ_B/Ce. Thus from the obtained effective magnetic moment, it is evident that the Ce atoms in $Ce_2Re_3Si_5$ are in a mixed valence state. This type of mixed valence state is not uncommon in Ce compounds. For example, $Ce_2Co_3Ge_5$ [29], $Ce_2Ni_3Si_5$ [30], Ce_2Rh_3Ge [31], and many other compounds exhibit the intermediate valence state of Ce [32,33]. The intermediate valence state of Ce and Yb atoms can be analyzed by a two-level ionic interconfiguration fluctuation (ICF) model [34].

We employed the model proposed by Franze *et al.* [35], which is a slightly modified version of the Sales and Wohlleben ICF model [34], to analyze the mixed valent nature of a Ce atom. According to this model, there exists a temperature associated with the fluctuations between the nonmagnetic $4f^0$ and magnetic $4f^1$ states, and the magnetic susceptibility is described by the fractional occupation of the two states. We have employed the following expression to analyze the temperature dependence of the magnetic susceptibility:

$$\chi(T) = \chi_0 + \left[(1-p)\chi_{ICF}(T) + p\left(\frac{C_{imp}}{T - \theta_p}\right) \right], \quad (1)$$

where χ_0 is the temperature-independent term that arises due to the diamagnetic susceptibility of the core electrons and the Pauli spin susceptibility of the conduction electrons; p separates the Ce ions that are in the mixed valent state and in the normal trivalent state; C_{imp} is the impurity configuration of Ce in the 3+ state; $\chi_{ICF}(T)$ is defined as

$$\chi_{ICF}(T) = \left(\frac{N}{3k_B}\right)\left[\frac{\mu_n^2 \nu(T) + \mu_{n-1}^2\{1 - \nu(T)\}}{\sqrt{(T^2 + T_{sf}^2)}} \right] \quad (2)$$

with

$$\nu(T) = \frac{2J_n + 1}{(2J_n + 1) + (2J_{n-1} + 1)\exp\left(\frac{E_{ex}}{k_B\sqrt{T^2 + T_{sf}^2}}\right)}, \quad (3)$$

where μ_n and μ_{n-1} are the effective moments of $4f^n$ and $4f^{n-1}$ states, and $(2\mathbf{J}_n + 1)$ and $(2\mathbf{J}_{n-1} + 1)$ are the degeneracies corresponding to the energy states E_n and E_{n-1}; and $E_{ex} = E_n - E_{n-1}$ is the interconfiguration excitation energy. T_{sf} is the spin fluctuation temperature, which is defined as
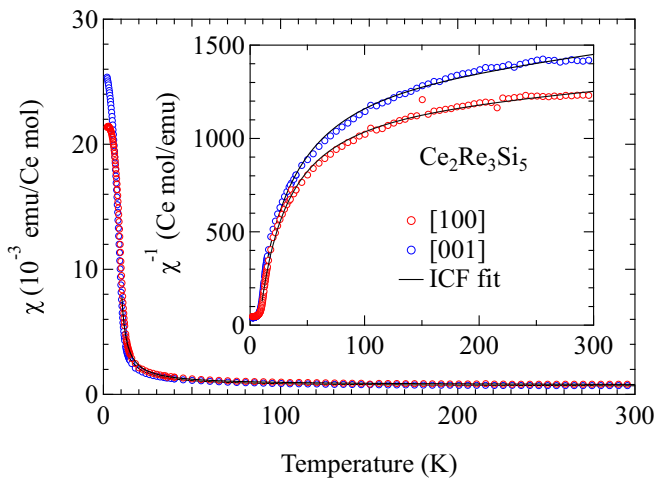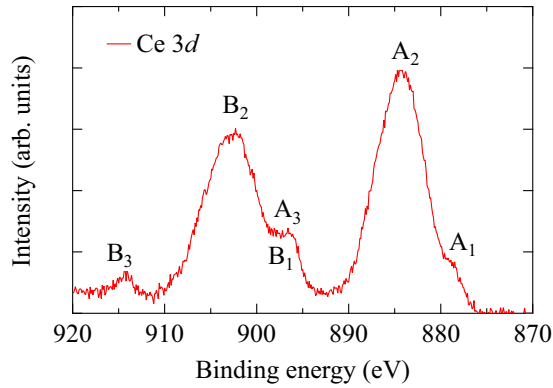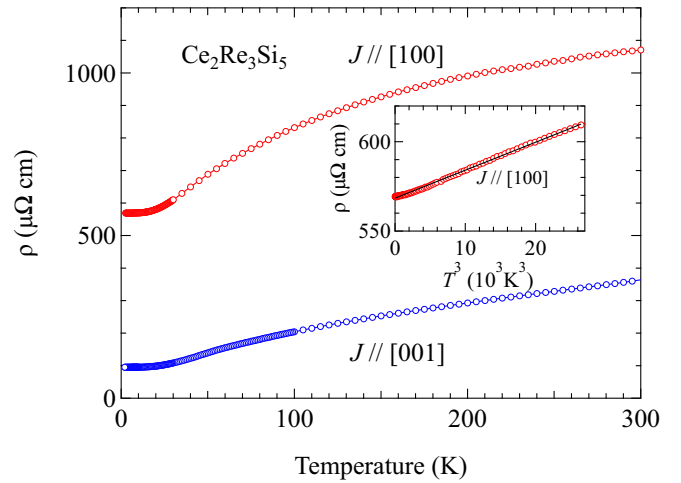
FIG. 3. Room-temperature Ce $3d$ XPS spectra of $Ce_2Re_3Si_5$.

FIG. 4. (a) Temperature dependence of electrical resistivity in the range 1.8–300 K for $J \parallel [100]$ and [001]. The inset shows the T^3 behavior of the electrical resistivity extending to a large temperature range for $J \parallel [100]$.

$T_{sf} = \hbar\omega_f/k_B$, where ω_f is the rate of fluctuation between $4f^n$ and $4f^{n-1}$ states, which essentially defines the $4f$ band. For Ce in the 4+ state ($J = 0; \mu = 0$) and for Ce in the 3+ state, ($J = 5/2; \mu = 2.54\,\mu_B$) and we fixed the C_{imp} term to 0.807 emu K/Oe mol. The fit to Eq. (1) is shown in Fig. 2 for the susceptibility and the inverse susceptibility as well. It is evident that the ICF model could very nicely explain the observed magnetic susceptibility with the following parameters: $\chi_0 = 8.97 \times 10^{-5}$ emu/mol, $p = 0.024$, $\theta_p = 7.68$ K for $H \parallel [100]$ and $\chi_0 = -4.97 \times 10^{-5}$ emu/mol, $n = 0.024$, $\theta_p = 5.96$ K for $H \parallel [001]$ for the Ce in a 3+ configuration and $E_{ex} = 454$ K, $T_{sf} = 920$ K for $H \parallel [100]$, $E_{ex} = 445$ K, and $T_{sf} = 872$ K for $H \parallel [001]$. A similar excitation energy has been observed in other Ce compounds [36–38], however the obtained value of T_{sf} in $Ce_2Re_3Si_5$ is much higher.

To confirm the mixed valent behavior of $Ce_2Re_3Si_5$, we have studied the Ce $3d$ core-level spectrum employing XPS. The experimental spectrum shown in Fig. 3 exhibits multiple features. The spectral region below 900 eV binding energy corresponds to the $3d_{5/2}$ photoemission signal, which is marked by A's. The corresponding spin-orbit-split $3d_{3/2}$ signal appears at higher binding energies and is denoted by B's in the figure. The presence of multiple features suggests significant final-state effects due to the hybridization of Ce $4f$ states with the conduction electronic states. Following the Gunnarsson-Schönhammer model, the feature A_1 appearing at 878 eV can be attributed to the well-screened final state, $|3d^9 4f^2\rangle$, where an electron from the conduction band has hopped to the $4f$ level at the photoemission site to screen the core hole [39–42]. The feature A_2 at 884 eV corresponds to the poorly screened state, $|3d^9 4f^1\rangle$. B_1 and B_2, which appear at 896 and 902 eV, respectively, are the corresponding spin-orbit-split features. In addition, there is a distinct intense feature at 914 eV denoted by B_3 that suggests the presence of the $|3d^9 4f^0\rangle$ final state, which is a signature of the Kondo feature. Clearly, the ground-state electronic configuration has a significant admixture of tetravalent ($|4f^0\rangle$) and trivalent ($|4f^1\rangle$) states. These results provide evidence of strong $4f$ hybridization with the conduction electronic states and the mixed valency of Ce in $Ce_2Re_3Si_5$.

The main panel of Fig. 4 illustrates the temperature dependence of electrical resistivity $\rho(T)$ of $Ce_2Re_3Si_5$ for current parallel to the [100] and [001] directions. The resistivity exhibits a metallic behavior with a large ρ_0 value at 2.0 K.

Usually, this type of large residual resistivity is attributed to the disorder in the crystal structure. However, from our SXRD it is clear that the grown crystals are perfectly ordered and all the sites are fully occupied. Hence the large residual resistivity may be attributed to the impurities or to the low carrier density as observed in CeP, Yb_4Sb_3, and Yb_4Bi_3 single crystals [43,44]. As expected, for a mixed valent system no magnetic transition is observed. A Fermi-liquid behavior is generally observed in the low-temperature region of the $\rho(T)$ of the valence fluctuating Ce-based intermetallic compounds [29,36]. However, in $Ce_2Re_3Si_5$, a T^3 behavior of electrical resistivity is observed as shown in the inset of Fig. 4(a). A similar behavior of T^3 in the low-temperature resistivity is observed in Eu-based valence fluctuating intermetallic compounds [45].

The temperature dependence of heat capacity $C_p(T)$ measured in zero field in the temperature range 2–300 K is shown in Fig. 5. As expected for a valence fluctuating compound, no anomalies in $C_p(T)$ have been observed down to 2 K.
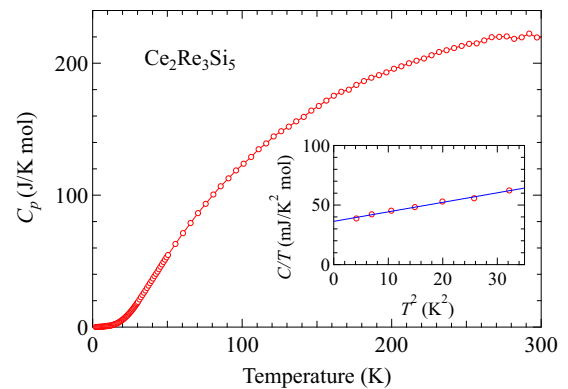
FIG. 5. (a) Temperature dependence of heat capacity $C_p(T)$ in the range 2–300 K. The inset shows the low-temperature data, plotted as C/T vs T^2. The solid line is a fit to estimate the Sommerfeld coefficient γ and the phononic term β of $Ce_2Re_3Si_5$.
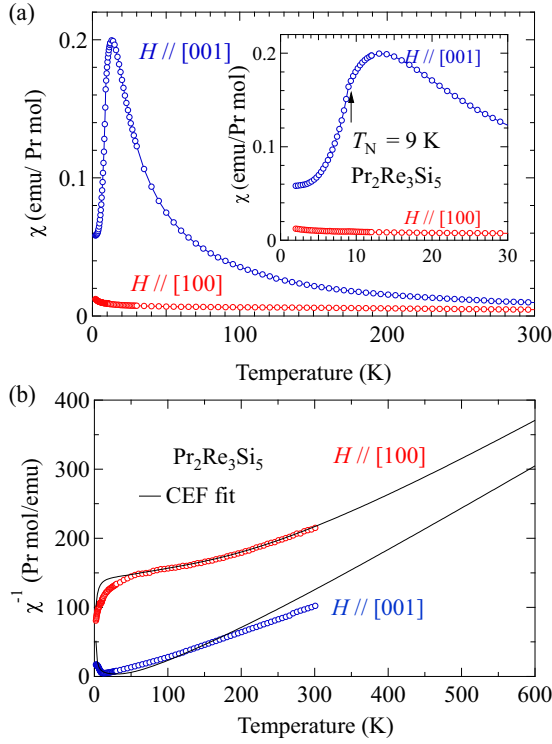
FIG. 6. (a) Temperature dependence of magnetic susceptibility of Pr$_2$Re$_3$Si$_5$ along the two principal crystallographic directions. The inset shows the low-temperature region of the magnetic susceptibility, which clearly depicts the magnetic ordering at $T_N = 9$ K. (b) The inverse susceptibility plot of Pr$_2$Re$_3$Si$_5$. The solid lines correspond to the CEF fit (see the text for details).

The low-temperature specific-heat data in the range 2–6 K plotted as C/T versus T^2 have been fitted to the expression $C(T)/T = \gamma + \beta T^2$, where γ is the electronic term and β is the phononic term. The best fit to the data is shown in the inset of Fig. 5 for $\gamma = 36$ mJ/K^2 mol and $\beta = 0.8$ mJ/K^4 mol. The estimated γ value is slightly larger than the conventional nonmagnetic metallic system, and this type of γ value has been observed in several other valence fluctuating Ce compounds. From the phononic term, one can calculate the Debye temperature Θ_D using the following expression:

$$\Theta_D = \left(\frac{12\pi^4 nR}{5\beta} \right)^{\frac{1}{3}}, \qquad (4)$$

where n is the number of atoms per formula unit, and R is the gas constant. The calculated Debye temperature for Ce$_2$Re$_3$Si$_5$ is 290 K.

C. Physical properties of Pr$_2$Re$_3$Si$_5$

The dc magnetic susceptibility of Pr$_2$Re$_3$Si$_5$ measured in the temperature range 2–300 K in a field of 1 kOe is shown in Fig. 6(a). A large anisotropy is observed in the magnetic susceptibility when the magnetic field is applied along the two principal crystallographic directions, viz., [100] and [001]. The susceptibility along the [100] direction possesses a small value and does not show a clear Curie-Weiss behavior as the temperature is decreased. At low temperature a kink is seen at $T_N = 9$ K (not shown here for brevity), below which it shows a very small upturn. On the other hand, along the [001] direction, the susceptibility increases more rapidly as the temperature is decreased from 300 K, and it shows a broad maximum below which at $T_N = 9$ K a sharp drop is observed similar to an antiferromagnetic transition. This suggests that the [001] direction is the easy axis of magnetization for Pr$_2$Re$_3$Si$_5$. The inverse magnetic susceptibility of Pr$_2$Re$_3$Si$_5$ is shown in Fig. 6(b). Once again, a large magnetocrystalline anisotropy is clearly visible in the inverse susceptibility plot. The Curie-Weiss fit to the paramagnetic regions of $\chi(T)^{-1}$ did not result in the effective magnetic moment corresponding to the 3+ valence state of Pr ($\mu_{eff} = 3.58\,\mu_B$/Pr). Thus Pr$_2$Re$_3$Si$_5$ does not obey the Curie-Weiss law in the temperature range up to 300 K, and this signals the fact that the overall crystal-field splitting of the $4f$-level is higher in this compound. A similar feature is observed in PrRh$_3$B$_2$ [46] and CeAgAs$_2$ [3], where the overall CEF splitting is much higher and the Curie-Weiss law is not obeyed in the temperature range below 300 K.

To understand the magnetocrystalline anisotropy and the overall CEF splitting, we analyzed $\chi(T)^{-1}$ based on the point-charge model [47]. The Pr atom in Pr$_2$Re$_3$Si$_5$ occupies the 8h Wyckoff position, which has a point symmetry m, which corresponds to monoclinic site symmetry. This indicates that $(2J+1)$ $(J=4)$ for Pr^{3+}, i.e., ninefold-degenerate levels will split into nine singlets. To get the energy eigenvalues and the eigenfunctions, we have used the following CEF Hamiltonian to estimate the CEF susceptibility:

$$\mathcal{H}_{CEF} = B_2^0 O_2^0 + B_2^2 O_2^2 + B_4^0 O_4^0 + B_4^2 O_4^2 + B_4^4 O_4^4$$
$$+ B_6^0 O_6^0 + B_6^2 O_6^2 + B_6^4 O_6^4 + B_6^6 O_6^6, \qquad (5)$$

where B_l^m and O_l^m are the crystal-field parameters and the Steven's operators [47,48], respectively. Here we have used the CEF Hamiltonian for orthorhombic site symmetry instead of monoclinic site symmetry, just to reduce the number of fitting parameters.

The CEF susceptibility is given by the expression

$$\chi_{CEFi} = N(g_J \mu_B)^2 \frac{1}{Z} \left(\sum_{m \neq n} | \langle m | J_i | n \rangle |^2 \frac{1 - e^{-\beta \Delta_{m,n}}}{\Delta_{m,n}} e^{-\beta E_n} + \sum_n | \langle n | J_i | n \rangle |^2 \beta e^{-\beta E_n} \right), \qquad (6)$$

where g_J is the Landé g-factor, and E_n and $|n\rangle$ are the nth eigenvalue and eigenfunction, respectively. J_i ($i = x$, y, and z) is a component of the angular momentum, and $\Delta_{m,n} = E_n - E_m$, $Z = \sum_n e^{-\beta E_n}$, and $\beta = 1/k_B T$. The magnetic susceptibility, including the molecular field contribution λ_i, is

given by

$$\chi_i^{-1} = \chi_{CEFi}^{-1} - \lambda_i. \qquad (7)$$

The inverse magnetic susceptibility calculated based on Eq. (7) is shown as solid lines in Fig. 6(b), which matches

TABLE II. CEF fit parameters, energy levels, and wave functions.

CEF parameters									
B_2^0 (K)	B_2^2 (K)	B_4^0 (K)	B_4^2 (K)	B_4^4 (K)	B_6^0 (K)	B_6^2 (K)	B_6^4 (K)	B_6^6 (K)	λ_i (emu/mol)$^{-1}$
-1.009	-0.0187	0.172	0.754	0.340	0.013	0.006	0.106	0.032	$\lambda_x = 43$, $\lambda_z = 64$

Energy levels				Wave functions				
E (K)	$\lvert 4\rangle$	$\lvert 3\rangle$	$\lvert 2\rangle$	$\lvert 1\rangle$	$\lvert 0\rangle$	$\lvert -1\rangle$	$\lvert -2\rangle$	$\lvert -3\rangle$	$\lvert -4\rangle$
---	---	---	---	---	---	---	---	---	---
1179	-0.570	0	-0.188	0	-0.526	0	-0.188	0	-0.570
1099	0.257	0	0.658	0	0	0	-0.658	0	-0.257
836	0	-0.032	0	-0.706	0	0.706	0	0.032	0
718	-0.658	0	0.257	0	0	0	-0.257	0	0.658
690	-0.001	0	0.631	0	-0.450	0	0.631	0	-0.001
598	0	0.074	0	0.703	0	0.703	0	0.074	0
163	0	0.703	0	-0.074	0	-0.074	0	0.703	0
2.75	0	0.706	0	-0.032	0	0.032	0	-0.706	0
0	0.417	0	-0.256	0	-0.721	0	-0.256	0	0.417

reasonably well to the experimentally observed data. The CEF parameters thus obtained are listed in Table II. The overall CEF splitting energy is 1179 K. Due to this large CEF splitting, the Curie-Weiss behavior is not obeyed for temperature below room temperature.

The field dependence of magnetization measured at a constant temperature $T = 2.0$ K along the two main crystallographic directions is shown in Fig. 7. The magnetization in the basal plane is weak and attains a small value in a magnetic field of 50 kOe. On the other hand, the magnetization along the c-axis increases gradually up to 35 kOe, at which point a sudden spin-flip-like metamagnetic transition is observed. The magnetization saturates at around 40 kOe to $2.92\,\mu_B$/Pr. Ideally, the saturation moment for Pr is $g_J \mathbf{J} = 3.2\,\mu_B$/Pr ($g_J = 4/5$ and $\mathbf{J} = 4$). We have analyzed the isothermal magnetization plot based on the CEF model with the following Hamiltonian:

$$\mathcal{H} = \mathcal{H}_{\text{CEF}} - g_J\mu_B \mathbf{J}_i(H + \lambda_i M_i), \quad (8)$$

where $\mathcal{H}_{\text{CEF}}$ is the CEF Hamiltonian defined in Eq. (5), and the second and third terms are the Zeeman term and the
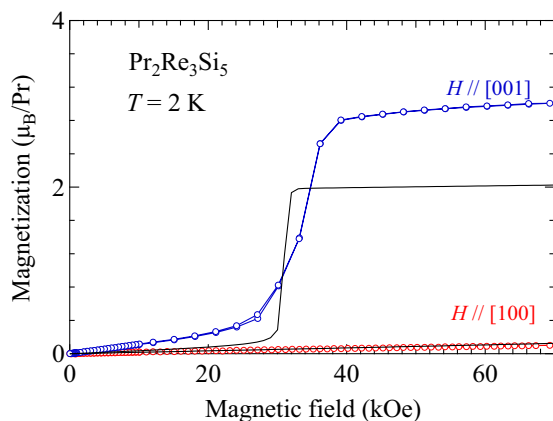
molecular field term, respectively. The magnetization M_i is defined as

$$M_i = g_J\mu_B \sum_n |\langle n|\mathbf{J}_i|n\rangle| \frac{\exp(-\beta E_n)}{Z} \quad (i = x, y, z). \quad (9)$$

The energy eigenvalues and eigenfunctions are obtained by diagonalizing the CEF Hamiltonian. The magnetization calculated from the parameters obtained from the inverse susceptibility plot qualitatively reproduces the experimental data. The easy axis and hard axis of magnetization are very well explained by the set of crystal-field parameters. However, the magnetization along the [001] direction is not quantitatively explained, but it may be attributed to the oversimplified point charge model.

To check the validity of crystal-field parameters and the obtained energy levels, we have estimated the magnetization value at 0 K for the exchange-induced ferromagnetic order in a Pr compound with a singlet CEF ground state [49], using the following expression:

$$m(T = 0\text{ K}) = 4g_J\mu_B\sqrt{1 - \tanh^2\left(\frac{\Delta}{2k_B T_C}\right)}, \quad (10)$$

where Δ is the energy difference between the ground state and the first excited state of the crystal-field-split levels, and T_C is the Curie temperature. Although this expression is for a ferromagnetic case, we have simply used this model to verify the validity of the estimated energy levels. Using $\Delta = 2.75$ K (see Table II) and $T_C = 9$ K, $m(T = 0\text{ K}) = 3.16\,\mu_B$ is obtained while experimentally we obtained a value of $2.9\,\mu_B$.

The temperature dependence of the heat capacity of Pr$_2$Re$_3$Si$_5$ is shown in the main panel of Fig. 8. It is evident from the figure that the heat capacity is approaching $3nR$ (= 250 J/K mol) at 300 K. The bulk nature of the magnetic ordering is visible by a sharp λ-like peak at low temperature. The low-temperature part of the heat capacity is shown in the bottom inset of Fig. 8(a). A sharp λ-like peak at $T = 9$ K confirms the magnetic ordering in this compound. The low-temperature heat capacity shows an upturn below 2.5 K, which may be attributed to the nuclear Schottky arising due
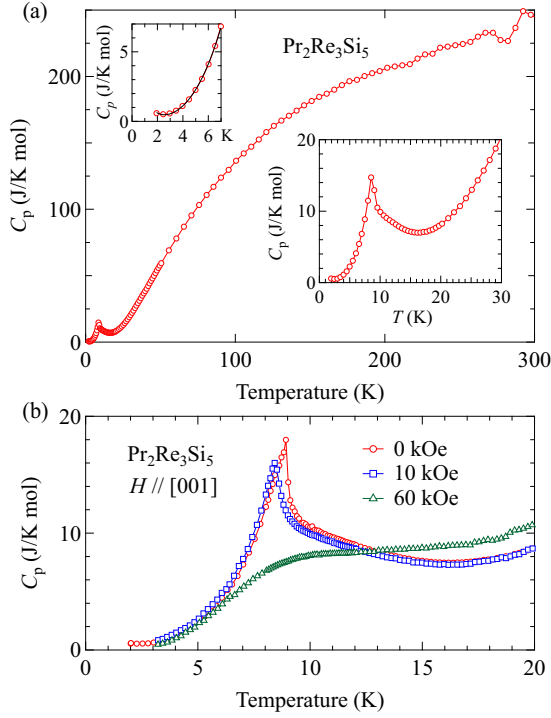

FIG. 7. Isothermal magnetization plots of Pr$_2$Re$_3$Si$_5$ along the two principal crystallographic directions measured at $T = 2$ K. The solid lines are the fits to the CEF model.

FIG. 8. (a) Temperature dependence of heat capacity of $Pr_2Re_3Si_5$ in the temperature range 2–300 K. The lower inset shows the low-temperature part of the heat capacity depicting the magnetic ordering at $T_N = 9$ K, and the top inset shows the low-temperature heat capacity with a nuclear Schottky fit (see the text for details). (b) Field dependence of the heat capacity.

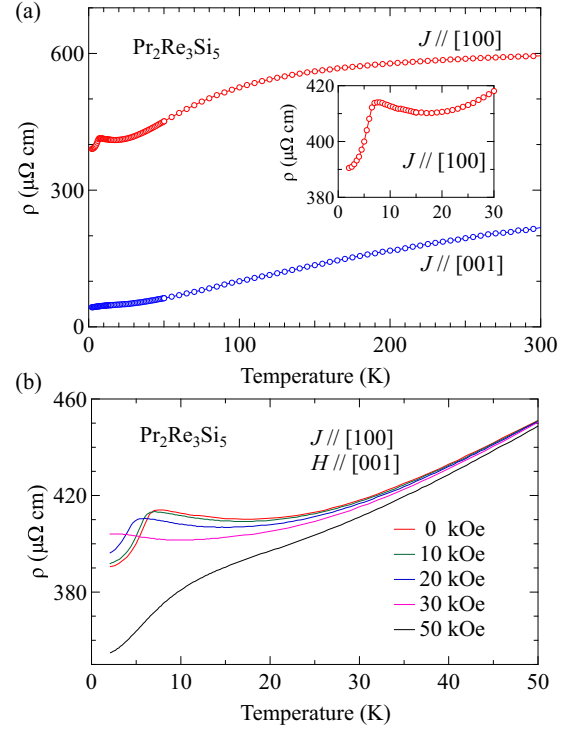FIG. 9. (a) Temperature dependence of electrical resistivity in the temperature range 1.8–300 K for $J \parallel$ [100] and [001]. The inset shows the low T behavior showing the antiferromagnetic ordering at $T_N = 9$ K. (b) Field dependence of electrical resistivity for $J \parallel$ [100] and $H \parallel$ [001].

to the interactions of the nuclear moments with $4f$ electrons. We fitted the low-temperature part of the heat capacity for $T \leqslant 4$ K to the following expression:

$$C_p = \gamma T + \beta T^3 + \left(\frac{C_N}{T^2}\right),\qquad(11)$$

where the first two terms are the usual electronic and lattice part of the heat capacity, and the third term is the nuclear Schottky heat capacity due to the hyperfine splitting of the nuclear spins. From the fitting, we have estimated the Sommerfeld coefficient $\gamma = 2.4$ mJ/K² mol, $\beta = 20.3$ mJ/K⁴ mol, and $C_N = 1105$ mJ/K mol. The β value of $Pr_2Re_3Si_5$ is larger than that of $Ce_2Re_3Si_5$, which suggests that this includes the antiferromagnetic magnon contribution as well, in addition to the phononic contribution. We obtain an estimation of the magnetic moment m_{4f} of Pr^{3+} from the nuclear heat capacity C_N using the following expression:

$$C_N = R A_{hf}^2 m_{4f}^2 \frac{I(I+1)}{3g_J^2},\qquad(12)$$

where R is the ideal gas constant, $A_{hf} \simeq 0.052$ K is the hyperfine coupling constant [50], and $I = 5/2$ is the nuclear spin for ^{141}Pr. Using these values and the estimated value of C_N in Eq. (12), the magnetic moment of Pr^{3+}, $m_{4f} = 3.2\,\mu_B/Pr$, is obtained, which is in close agreement with the experimental value of the saturation moment $2.9\,\mu_B/Pr$. We have also measured the field dependence of heat capacity of $Pr_2Re_3Si_5$ as

shown in Fig. 8(b). When the applied field is parallel to the easy axis of magnetization, viz., [001], the T_N shifts toward lower temperature, and for fields above 40 kOe there is a broad humplike feature suggesting the field-induced ferromagnetic state as observed in Fig. 7.

The temperature dependence of electrical resistivity for current along the two principal crystallographic directions is shown in Fig. 9(a). As expected, there is a large anisotropy in the $\rho(T)$ reflecting the tetragonal crystal structure. At room temperature, $\rho(T)$ attains a value of about 600 $\mu\Omega$ cm for $J \parallel$ [100]. As the temperature is decreased, the resistivity gradually decreases and shows a broad maximum centered around 120 K and then a very subtle upturn before it drops at $T_N = 9$ K, where the antiferromagnetic ordering sets in and hence there is a reduction in spin disorder scattering. The broad maximum at around 120 K may simply be attributed to the thermal population of the CEF levels. As observed in $Ce_2Re_3Si_5$, the residual resistivity is high even for $Pr_2Re_3Si_5$. We have also measured the electrical resistivity under applied magnetic fields, as shown in Fig. 9(b). The magnetic field is applied along the easy axis of magnetization [001] direction. With the increase in the magnetic field, T_N decreases and is not discernible for fields greater then 40 kOe. This type of behavior is typically observed in antiferromagnetic compounds. The residual resistivity decreases with increasing magnetic field, thus indicating the suppression of spin fluctuation by an applied field as the antiferromagnetic compounds are entering into a field-induced ferromagnetic state.

IV. SUMMARY

We have successfully grown the single crystals of $Ce_2Re_3Si_5$ and $Pr_2Re_3Si_5$ by the Czochralski method. From the magnetic and transport property measurements it is obvious that no magnetic transition is observed down to 2 K in $Ce_2Re_3Si_5$. Furthermore, the magnetic susceptibility and the crystal structure (unit cell volume) lend credence to the nonmagnetic valence fluctuating state of $Ce_2Re_3Si_5$. The ICF model explains the $\chi(T)$ behavior and confirms the valence fluctuating nature in $Ce_2Re_3Si_5$, which is also substantiated by the XPS studies. $Pr_2Re_3Si_5$, on the other hand, undergoes an antiferromagnetic transition at 9 K which is confirmed both from the magnetic and the transport data. Heat capacity data also confirmed the bulk nature of the magnetic ordering in $Pr_2Re_3Si_5$. The easy axis of magnetization was found to be [001]. We have performed the CEF analysis on the magnetic susceptibility and magnetization data. From the analysis

it is clear that the overall crystal-field splitting is large in $Pr_2Re_3Si_5$. Although our CEF levels to a large extent explain the magnetic susceptibility and magnetization, inelastic neutron scattering experiments are necessary to confirm these energy levels.

[1] Y. Ōnuki, *Physics of Heavy Fermions: Heavy Fermions and Strongly Correlated Electrons Systems* (World Scientific, Singapore, 2018).

[2] J. Jensen and A. R. Mackintosh, *Rare Earth Magnetism* (Clarendon, Oxford, 1991).

[3] R. Mondal, R. Bapat, S. K. Dhar, and A. Thamizhavel, Phys. Rev. B **98**, 115160 (2018).

[4] R. Parks, Hyperfine Interact. **25**, 565 (1985).

[5] Y. Onuki, R. Settai, K. Sugiyama, T. Takeuchi, T. C. Kobayashi, Y. Haga, and E. Yamamoto, J. Phys. Soc. Jpn. **73**, 769 (2004).

[6] P. Coleman, C. Pépin, Q. Si, and R. Ramazashvili, J. Phys.: Condens. Matter **13**, R723 (2001).

[7] Q. Si and F. Steglich, Science **329**, 1161 (2010).

[8] P. Gegenwart, Q. Si, and F. Steglich, Nat. Phys. **4**, 186 (2008).

[9] V. Anand, Z. Hossain, D. Adroja, C. Geibel *et al.*, J. Phys.: Condens. Matter **23**, 276001 (2011).

[10] A. Yatskar, W. P. Beyermann, R. Movshovich, and P. C. Canfield, Phys. Rev. Lett. **77**, 3637 (1996).

[11] R. Gumeniuk, W. Schnelle, H. Rosner, M. Nicklas, A. Leithe-Jasper, and Y. Grin, Phys. Rev. Lett. **100**, 017002 (2008).

[12] K. Mitsumoto, S. Goto, Y. Nemoto, M. Akatsu, T. Goto, N. D. Dung, T. D. Matsuda, Y. Haga, T. Takeuchi, K. Sugiyama *et al.*, J. Phys.: Condens. Matter **25**, 296002 (2013).

[13] D. E. Bugaris, C. D. Malliakas, F. Han, N. P. Calta, M. Sturza, M. J. Krogstad, R. Osborn, S. Rosenkranz, J. P. Ruff, G. Trimarchi *et al.*, J. Am. Chem. Soc. **139**, 4130 (2017).

[14] S. Ramakrishnan, A. Schönleber, T. Rekis, N. van Well, L. Noohinejad, S. van Smaalen, M. Tolkiehn, C. Paulmann, B. Bag, A. Thamizhavel, D. Pal, and S. Ramakrishnan, Phys. Rev. B **101**, 060101(R) (2020).

[15] A. Thamizhavel, H. Nakashima, Y. Obiraki, M. Nakashima, T. D Matsuda, Y. Haga, K. Sugiyama, T. Takeuchi, R. Settai, M. Hagiwara *et al.*, J. Phys. Soc. Jpn. **74**, 2843 (2005).

[16] M. Nakashima, H. Kohara, A. Thamizhavel, T. Matsuda, Y. Haga, M. Hedo, Y. Uwatoko, R. Settai, and Y. Ōnuki, J. Phys.: Condens. Matter **17**, 4539 (2005).

[17] R. Feyerherm, B. Becker, M. Collins, J. Mydosh, G. Nieuwenhuys, and S. Ramakrishnan, Phys. B **241–243**, 643 (1997).

[18] Z. Hossain, H. Ohmoto, K. Umeo, F. Iga, T. Suzuki, T. Takabatake, N. Takamoto, and K. Kindo, Phys. Rev. B **60**, 10383 (1999).

[19] Y. Singh, D. Pal, and S. Ramakrishnan, Phys. Rev. B **70**, 064403 (2004).

[20] D. Huo, J. Sakurai, T. Kuwai, T. Mizushima, and Y. Isikawa, Phys. Rev. B **65**, 144450 (2002).

[21] N. H. Sung, C. J. Roh, K. S. Kim, and B. K. Cho, Phys. Rev. B **86**, 224507 (2012).

[22] E. Parthe and B. Chabot, Handb. Phys. Chem. Rare Earths **6**, 113 (1984).

[23] See Supplemental Material at http://link.aps.org/supplemental/10.1103/PhysRevB.105.165134 for details on the single-crystal x-ray diffraction analysis.

[24] J. Rodríguez-Carvajal, Phys. B **192**, 55 (1993).

[25] O. Bodak, V. Pecharskii, and E. Gladyshevskii, Inorg. Mater. **14**, 188 (1978).

[26] W. Jeitschko and M. Schlüter, Z. Anorg. Allg. Chem. **636**, 1100 (2010).

[27] APEX-III, APEX III software, Bruker Axs Inc., Madison, WI (2013).

[28] V. Petricek, V. Eigner, M. Dusek, and A. Cejchan, Z. Kristallogr. **231**, 301 (2016).

[29] S. Layek, V. Anand, and Z. Hossain, J. Magn. Magn. Mater. **321**, 3447 (2009).

[30] C. Mazumdar, R. Nagarajan, S. K. Dhar, L. C. Gupta, R. Vijayaraghavan, and B. D. Padalia, Phys. Rev. B **46**, 9009 (1992).

[31] M. Falkowski and A. Strydom, J. Phys.: Condens. Matter **27**, 395601 (2015).

[32] V. Babizhetskyy, O. Isnard, and K. Hiebl, Solid State Commun. **142**, 80 (2007).

[33] M. Falkowski and A. Strydom, J. Alloys Compd. **883**, 160925 (2021).

[34] B. Sales and D. Wohlleben, Phys. Rev. Lett. **35**, 1240 (1975).

[35] W. Franz, F. Steglich, W. Zell, D. Wohlleben, and F. Pobell, Phys. Rev. Lett. **45**, 64 (1980).

[36] U. B. Pramanik, Anupam, U. Burkhardt, R. Prasad, C. Geibel, and Z. Hossain, J. Alloys Compd. **580**, 435 (2013).

[37] M. Falkowski and L. Horák, J. Alloys Compd. **773**, 462 (2019).

[38] M. Mihalik, M. Diviš, and V. Sechovský, Phys. B **404**, 3191 (2009).

[39] F. De Groot and A. Kotani, *Core Level Spectroscopy of Solids* (CRC, Boca Raton, FL, 2008).

[40] O. Gunnarsson and K. Schönhammer, Phys. Rev. B **28**, 4315 (1983).

[41] M. B. Gamża, R. Gumeniuk, U. Burkhardt, W. Schnelle, H. Rosner, A. Leithe-Jasper, and A. Ślebarski, Phys. Rev. B **95**, 165142 (2017).

[42] N. Sahadev, D. N. Biswas, S. Thakur, and K. Ali, in *Solid State Physics: Proceedings of the 57th DAE Solid State Physics Symposium 2012*, edited by A. K. Chauhan, Chitra Murli, and S. C. Gadkari, AIP Conf. Proc. 1512 (AIP, Melville, NY, 2013), pp. 828–829.

[43] Y. Kwon, Y. Haga, O. Nakamura, T. Suzuki, and T. Kasuya, Phys. B **171**, 324 (1991).

[44] A. Ochiai, T. Suzuki, and T. Kasuya, J. Phys. Soc. Jpn. **59**, 4129 (1990).

[45] S. Patil, R. Nagarajan, L. Gupta, B. Padalia, and R. Vijayaraghavan, Solid State Commun. **76**, 1173 (1990).

[46] M. Yamada, Y. Obiraki, T. Okubo, T. Shiromoto, Y. Kida, M. Shiimoto, H. Kohara, T. Yamamoto, D. Honda, A. Galatanu *et al.*, J. Phys. Soc. Jpn. **73**, 2266 (2004).

[47] M. T. Hutchings, in *Solid State Physics* (Elsevier, Amsterdam, 1964), Vol. 16, pp. 227–273.

[48] K. Stevens, Proc. Phys. Soc. Sect. A **65**, 209 (1952).

[49] P. Fazekas, *Lecture Notes on Electron Correlation and Magnetism* (World Scientific, Singapore, 1999), Vol. 5.

[50] J. Kondo, J. Phys. Soc. Jpn. **16**, 1690 (1961).